nature physics

ARTICLES

https://doi.org/10.1038/s41567-019-0506-8

Scaling laws indicate distinct nucleation mechanisms of holes in the nuclear lamina

Dan Deviri[1*], Charlotte R. Pfeifer[2,3], Lawrence J. Dooling[2], Irena L. Ivanovska[2], Dennis E. Discher[2,3] and Samuel A. Safran[1]

During a first-order phase transition, an interfacial layer is formed between the coexisting phases and kinetically limits homogeneous nucleation of the new phase in the original phase. This inhibition is commonly alleviated by the presence of impurities, often of unknown origin, that serve as heterogeneous nucleation sites for the transition. Living systems present a theoretical opportunity: the regulated structure of living systems allows modelling of the impurities, enabling quantitative analysis and comparison between homogeneous and heterogeneous nucleation mechanisms, usually a difficult task. Here, we formulate an analytical model of heterogeneous nucleation of holes in the nuclear lamina, a phenomenon with implications in cancer metastasis, ageing and other diseases. We then present measurements of hole nucleation in the lamina of nuclei migrating through controlled constrictions and fit the experimental data to our heterogeneous nucleation model as well as a homogeneous model. Surprisingly, we find that different mechanisms dominate depending on the density of filaments that comprise the nuclear lamina.

A stable system may transform into a metastable one with the variation of external fields (for example, temperature, pressure, mechanical stresses). Transition from the metastable state to the new, globally stable state of the system is often inhibited by a kinetic energy barrier related to the interfacial tension between the phases. Small volumes of the stable (lower free energy) state can be nucleated by fluctuations, but surface tension promotes the shrinking and disappearance of droplets whose radii are smaller than a critical radius[1]. Nucleation may be slow, depending on the magnitude of the kinetic energy barrier, which generally correlates with the interfacial surface tension. Phase transitions that are kinetically limited by nucleation are ubiquitous, including crystallization, vaporization, condensation, cavitation and chemical reactions[2,3]. The required nucleation could be homogeneous, or heterogeneous at sites of impurities or defects. The theoretical treatment of homogeneous nucleation is relatively simple because it requires only the formulation of the intrinsic (defect-free) free energy landscape of the system. On the other hand, heterogeneous nucleation, which commonly dominates the kinetics, requires detailed characterization of the defects. Their nature and characteristics are unknown or too complex in most systems, which makes quantitative, predictive theories very difficult to formulate.

Hole nucleation in two-dimensional (2D) layers, which is the 2D analogue of cavitation, is relevant to the important problem of mechanically induced deformations of the cell nucleus (which can lead to genetic changes)[4,5]. In this Article we take advantage of the regular structure of the cell nucleus[6] (see Supplementary Information for details) to identify and physically characterize the energetics of the defects that promote heterogeneous nucleation of holes. We formulate a quantitative theory that predicts the rate of hole nucleation, its crossover to homogeneous nucleation, and present experimental data that show how the two different mechanisms are manifested in different cell types.

Nuclei are commonly deformed due to migration through narrow constrictions in tissues or, even in the absence of migration, due to contractility of the cell actin cytoskeleton itself. The nuclear envelope (NE), which includes two lipid bilayer membranes, separates the nucleus from the cytoplasm. A biopolymer, gel-like layer known as the lamina is connected to the inner nuclear membrane of the NE and reinforces it (Fig. 1a) via protein linkers. Mechanical deformations of the nucleus may lead to the formation of nuclear membrane protrusions known as blebs, which form by detachment of the NE from the lamina or lamina holes nucleation (see 'Nuclear blebs and chromatin herniation' in the Supplementary Information). In both scenarios, the excess inner pressure, which is no longer balanced by the lamina, inflates the NE and forms a bleb[7,8] (Fig. 2). Here, we focus on the mechanisms of lamina hole nucleation, which may lead to blebbing and subsequent chromatin (DNA and associated proteins) herniation into the bleb and thus to organizational changes of the DNA. In this case, bleb bursting (unregulated NE rupture) can lead to DNA damage which may cause genetic changes[4,5,9,10]. Understanding the dependence of in vivo lamina hole nucleation on the relevant biological parameters (for example, protein synthesis, enzymatic activity) may inform future research focused on diseases that are related to nuclear or cellular blebbing, including cancer (see 'Nuclear blebs and chromatin herniation' in the Supplementary Information). Existing theoretical models for hole nucleation in soft matter (such as vesicles[11]) assume that the stretched layer is a homogeneous, linear-elastic material, which allows one to relate the rate of hole nucleation to lateral stresses and strains. The predicted scaling relations for the probability of hole nucleation as a function of strain successfully match experimental measurements of hole nucleation in homogeneous, lipid bilayer vesicles[12]. Here, we show that this can be applicable to lamina hole nucleation and blebbing, but only for certain conditions and cell types.

In other cell types, the homogeneous nucleation mechanism fails to predict the observed scaling of the probability of bleb formation with deformation-related strain. In contrast to the models studied in the context of vesicles, biological membranes and layers

[1]Department of Chemical and Biological Physics, Weizmann Institute of Science, Rehovet, Israel. [2]Biophysical Engineering Labs, University of Pennsylvania, Philadelphia, PA, USA. [3]Graduate Group/Department of Physics & Astronomy, University of Pennsylvania, Philadelphia, PA, USA. *e-mail: dan.deviri@Weizmann.ac.il

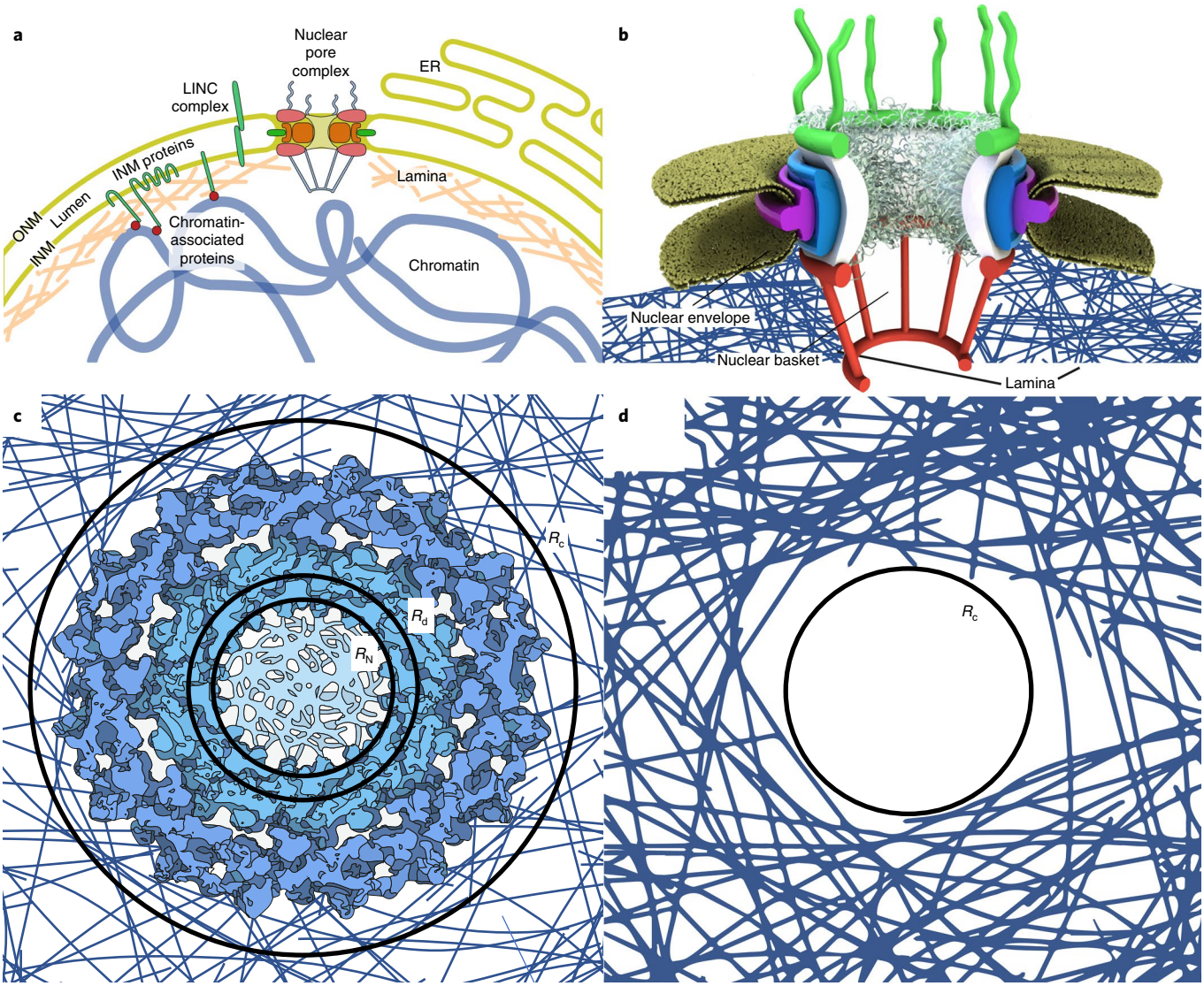

Fig. 1 | Structure and heterogeneities of the nuclear lamina. a, The nucleus, comprising chromatin (DNA and binding proteins) bounded by the nuclear envelope (NE), a complex of two lipid bilayers separated by a volume that is contiguous with the lumen of the endoplasmic reticulum (ER; perinuclear space). The NE, which contains embedded nuclear pore complexes (NPCs) and chromatin-associated proteins, is attached, on its inner side, to the nuclear lamina. ONM, outer nuclear membrane; INM, inner nuclear membrane. **b**, Side view of the NPC and its lamina-associated substructure, the nuclear basket. **c**, Top view of the NPC (surrounded by the lamina, which is tethered to the nuclear basket). The nuclear basket and the associated lamin filaments are an example of a heterogeneous nucleation site, denoted as a BLasket. The circles denote the three radii defined in the model, R_c, R_d and R_N, which represent the critical nucleation radius, the BLasket disassembly radius and BLasket equilibrium radius, respectively. The critical nucleation radius is depicted as being greater than the disassembly radius, but it may be smaller with high enough strain. **d**, Hole nucleation in the homogeneous part of the lamina. Figure adapted from **a**, ref. [22]; **b**, ref. [23]; **c**, ref. [24], under a Creative Commons licence (https://creativecommons.org/licenses/by/4.0/).

are not homogeneous, but are heterogeneous due to embedded protein complexes. Motivated by this, we present a general theory for hole nucleation in heterogeneous, thin films that takes into account the elastic properties of defects, such as protein complexes, which may serve as nucleation sites for holes. The scaling law predicted by our theory, when applied to the lamina, relates the lamina hole nucleation rate to lateral strain, and is fundamentally different from the homogeneous case. In addition, we present new experiments that use a constricted migration assay of a symmetric, cylindrical geometry that allows accurate estimations of the lateral strain of the lamina of migrating nuclei and high-throughput, precise measurements of blebbing fractions (Fig. 3). This allows us to quantitatively compare the experiments with the predictions of the scaling laws of lamina hole nucleation as a function of strain for the homogeneous versus heterogeneous mechanisms (Fig. 4). We find that cells with a high density of lamina filaments satisfy scaling laws predicted for heterogeneous nucleation, while cells with low-density laminae satisfy the scaling law predicted for homogeneous nucleation. This correlation of bleb formation as a function of strain with different laminae densities characteristic of different cell types suggests that blebbing may indeed be caused by failure of the lamina layer, which can occur via two physically distinct mechanisms.

Model predictions

Homogeneous hole nucleation. We begin by recalling previous theory[11] that analysed the kinetics of hole nucleation in vesicles as a homogeneous nucleation problem. The line tension γ that inhibits the nucleation of holes was introduced phenomenologically, and the

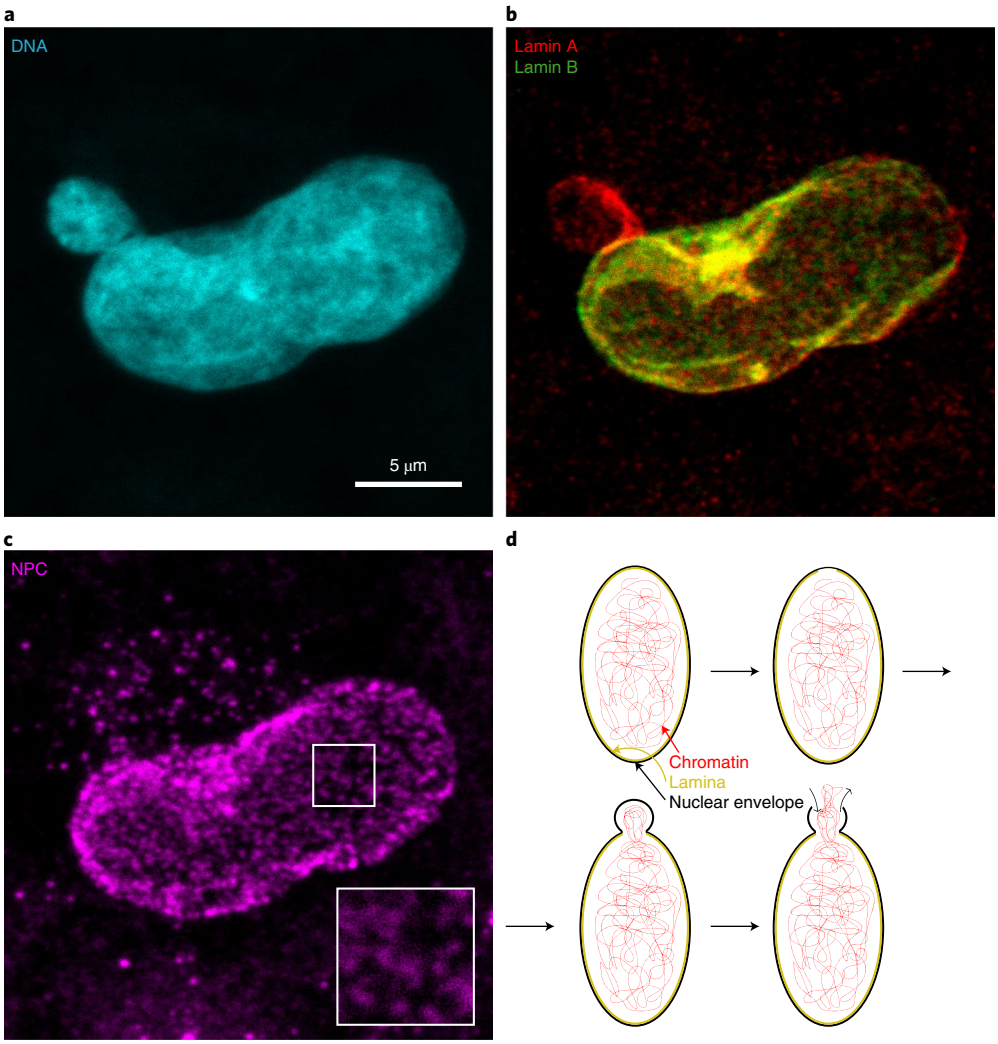

Fig. 2 | Exclusion of NPCs and lamina from the chromatin-rich bleb. a–c, A cell was fixed after migrating through Transwell pores and its nucleus was stained for chromatin (**a**), lamin A and B (**b**) and NPCs (**c**). The nucleus shows the formation of a bleb, which contains chromatin and lamin A but not lamin B or NPCs. **d**, Heuristic model for bleb formation due to lamina hole nucleation[7].

energy barrier for homogeneous nucleation of hole was calculated. Under the assumption that holes nucleate due to noise (for example, thermal fluctuations, active processes), the rate of hole nucleation Γ can be written as

$$\Gamma \sim e^{-\frac{\beta\pi\gamma^2}{E\varepsilon}} \tag{1}$$

where β^{-1} is the magnitude of the noise[13], E is the 2D Young's modulus and ε is the lateral strain of the deformed layer. The predicted log of the nucleation rate then varies inversely with the applied strain. For a review of the derivation of equation (1) see Supplementary Information.

Heterogeneous hole nucleation. We now calculate the energy barrier for heterogeneous nucleation of holes in the nuclear lamina. The lamina layer contains heterogeneities[7] (for example, embedded proteins) that, when stressed, serve as nucleation sites for holes that can lead to blebbing. Because the NPC is the largest nuclear protein complex (see Supplementary Information for detailed background), it is very likely that its lamina-associated structure, the nuclear basket, serves as a major nucleation site. To account for the nuclear Basket as well as its tethers to the Lamin filaments (Fig. 1) (which is distinct from the homogeneous region of the lamina structure), we generically refer to these heterogeneities as BLaskets; however, we stress that our theory is applicable for any protein complex or lamina heterogeneity[7]. Based on the structure of the nuclear basket[14], we model these BLaskets as circular areas of perturbed lamina, which tend to resist changes in their size. However, under sufficiently large stress, BLaskets can fail and result in lamina holes. We thus model the energy of a BLasket as a function of its effective radius, by a harmonic potential that is truncated at a specific disassembly radius R_d:

$$U_{BL}(R) = \begin{cases} -B + \alpha (R - R_N)^2 & R \le R_d \\ 0 & R > R_d \end{cases} \tag{2}$$

The sharp cutoff at R_d is only an approximation for mathematical simplicity.

Here, $B > 0$ accounts for the cohesive energy of BLasket proteins in their unstrained state, R_N is the BLasket radius in the absence of any external deformations, and the phenomenological 'spring constant' α accounts for the mechanical response of the BLasket. Heterogeneous nucleation of a hole is driven by expansion and disassembly of BLaskets. We are therefore interested in the energy difference between the state in which the BLasket is expanded and the

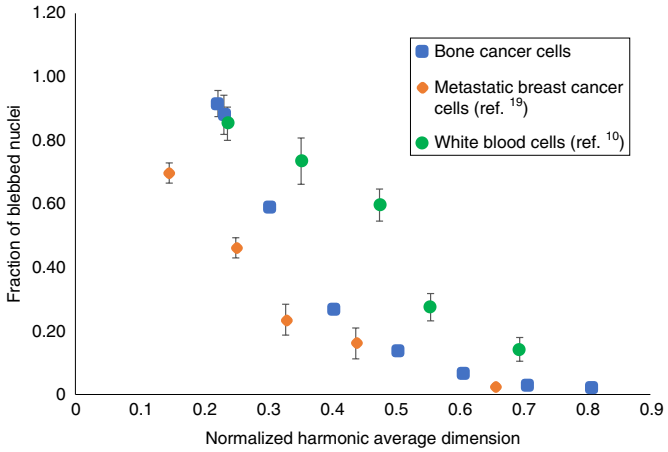

Fig. 3 | Fraction of the blebbed or NE ruptured nuclei φ plotted against the harmonic average of the constriction dimensions r. Note that $r=(r_1^{-1}+r_2^{-1})^{-1}$, where $r_{1,2}$ are the constriction dimensions and r is the harmonic average. This type of averaging accounts for the curvatures imposed by the constrictions rather than the dimensions, and is thus more physically significant. To account for differences in nuclear sizes among different cell types, the averages were normalized by the radius of the nuclei of suspended cells of the appropriate type (see 'Strain estimates' in the Supplementary Information). The data for white blood cells and metastatic breast cancer cells are taken from refs. [10] and [19], respectively. Centre lines and box limits represent average values and error bars (s.e.m.), respectively. Error bars for the bone cancer cell data points are of the order of the size of the points. Horizontal s.e.m. values are based on $N=40$ measurements. Vertical s.e.m. values are based on sample sizes of 68, 53, 363, 389, 1,100, 274, 289 and 601 for the 2.2, 2.3, 3.0, 4.0, 5.0, 6.0, 7.0 and 8.0 μm pores, respectively. All measurements are relative to the average fraction of blebbed nuclei in cells before constricted migration (1.08 ± 0.3% based on $N=1{,}115$ samples). Errors of NE ruptured fractions of white blood cells and metastatic breast cancer cells are taken from refs. [10] and [19], respectively. Errors for the constriction dimensions of white blood cells and metastatic breast cancer cells data are not shown, as these were not reported.

state in which the BLasket is at its undeformed radius R_N. Expansion of the BLasket costs energy due to its harmonic response to changes in its radius, but it also reduces the overall system energy in the presence of applied tension. If the BLasket is expanded to the extent that its radius $R>R_d$, it disassembles, resulting in a hole (which might be of subcritical radius[15]) whose energetics are determined by the homogeneous elastic energy of the lamina and its line tension. The sum of the BLasket deformation energy (or line tension if it disassembles) and the contribution due to partial relaxation of the lamina elastic energy results in the following expression for the total lamina energy difference as a function of the BLasket radius (see Supplementary Information):

$$\Delta U(R) = \begin{cases} -\varepsilon\pi E(R^2-R_N^2)+\alpha(R-R_N)^2 & R\le R_d \\ -\varepsilon\pi E(R^2-R_N^2)+2\pi\gamma(R-R_d)+\alpha(R_d-R_N)^2 & R>R_d \end{cases} \quad (3)$$

In our model for heterogeneous nucleation of the lamina hole, disassembly of a BLasket is a necessary first step in lamina hole nucleation; this is defined as formation of a hole large enough that the line tension does not inhibit its further growth[15]. This occurs when the hole radius R is greater than both the disassembly radius R_d and the critical, homogeneous, nucleation radius $R_c=\gamma/(E\varepsilon)$. R_c decreases with lamina strain ε while R_d is strain-independent. Thus, the equation $R_c=R_d$ defines a critical strain $\varepsilon_c=\gamma/(ER_d)$. The critical strain ε_c defines two regimes that are physically distinct: in the low-strain regime $\varepsilon<\varepsilon_c$, disassembly of the BLasket forms a subcritical hole and lamina holes will be nucleated if the subcritical hole expands to the extent that its radius is greater than R_c (Fig. 1c). In this regime, the log of the nucleation probability scales approximately inversely with the imposed strain, similar to hole nucleation in homogeneous layers (equation (1)), because the BLasket plays only a secondary role in the nucleation process (see Supplementary Information). We next focus on the high-strain regime $\varepsilon>\varepsilon_c$, in which the rate-limiting step of nucleation is the disassembly of the BLasket, without necessarily involving expansion of a subcritical hole. This heterogeneous nucleation regime qualitatively changes the scaling of the log of the nucleation rate with the strain from $1/\varepsilon$ (homogeneous nucleation) to an approximately linear relationship, which we now quantify in more detail.

In the presence of finite strain, $R=R_N$ is no longer the equilibrium size of the BLasket, which grows in response to the applied stress as described by minimization of the energy (equation (3)) in the regime $R\le R_d$. The new equilibrium BLasket radius $\widetilde{R}_N(\varepsilon)$ is (see Supplementary Information) given by

$$\widetilde{R}_N(\varepsilon)\approx\frac{R_N}{1-\varepsilon\frac{\pi E}{\alpha}} \quad (4)$$

It is important to note that as we expect R_d (an upper limit on $\widetilde{R}_N$) to be of the same order of magnitude as R_N, the singularity at $\pi\varepsilon E/\alpha=1$ cannot be reached physically.

The energy barrier ΔE_d for disassembly of the BLasket is simply the difference between the total energy of a BLasket of radius R_d and one of radius $\widetilde{R}_N$. This is calculated from equation (3) (see Supplementary Information):

$$\Delta E_d\approx\alpha(R_d-R_N)^2-\varepsilon\pi ER_d^2+\frac{\varepsilon\pi ER_N^2}{1-\varepsilon\frac{\pi E}{\alpha}} \quad (5)$$

The rate of heterogeneous hole nucleation Γ is therefore

$$\Gamma(\varepsilon)\sim\begin{cases}\exp\left(-\beta\frac{\pi\gamma^2}{\varepsilon E}\right) & \varepsilon<\varepsilon_c \\ \exp\left(\beta\varepsilon\pi ER_d^2-\frac{\beta\varepsilon\pi ER_N^2}{1-\varepsilon\pi E/\alpha}\right) & \varepsilon\ge\varepsilon_c\end{cases} \quad (6)$$

where β^{-1} is the magnitude of the noise. It is important to note that, although the theory above is written in terms of a single BLasket, it can be easily generalized to many (non-interacting and uniform) BLaskets without any change to equations (5) and (6) (see Supplementary Information).

Application to experiments

Heterogeneous and homogeneous nucleations of holes in the lamina layer are qualitatively different. Heterogeneous hole nucleation is the result of localized stresses that act to disassemble an existing BLasket, which subsequently creates a hole that may continue to grow. In this case, the energy barrier is primarily associated with the disassembly energy, which, in turn, depends on the stresses exerted by the lamina on the BLasket. In the framework of linear elasticity, these localized stresses are proportional to the imposed (either externally or via intrinsic, cellular contractility) strain, ε. The imposed stresses expand the BLasket, making the (mechanical) equilibrium BLasket radius $\widetilde{R}_N$ closer to the disassembly radius R_d, so that the disassembly energy (described by equation (5)) decreases

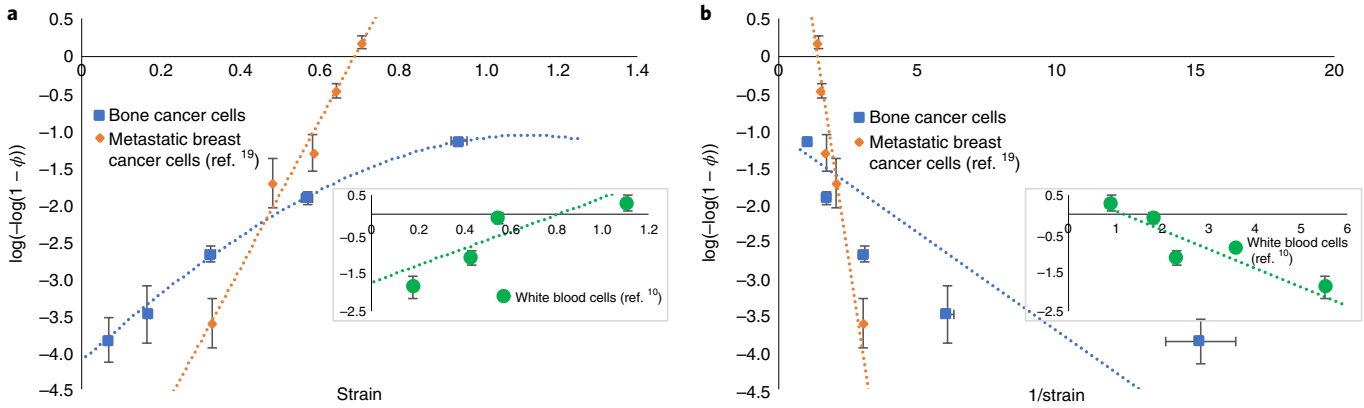

Fig. 4 | Fit to the experimental data. Fit of the data points expected to be within the linear elastic regime of the lamina (see Supplementary Information; for full data see Supplementary Fig. 2a) to the predicted scaling for the strain dependence of the transformed fraction of blebbed or NE ruptured nuclei ϕ (see section 'Data fit' in the Methods) of the two nucleation mechanisms. **a**, Fit of the data to the scaling law predicted for localized disassembly of a BLasket (appropriate for large strains, $\varepsilon > \varepsilon_c$) by equation (6). The data collected from different cell types show different qualities of fit: data for bone cancer cells (U2OS, blue) fit well while data of metastatic breast cancer cells (MDA-MB-231, orange) and white blood cells (hDC, green) fit poorly compared with the fit to the predicted scaling of the homogeneous nucleation mechanism (shown in **b**). **b**, Fit of the data to the scaling with the inverse of the strain, predicted by the theory for homogeneous nucleation: data of U2OS cells (blue) fit very poorly while data of MDA-MB-231 (orange) and hDC (inset, green) cells fit reasonably. Data for white blood cells and metastatic breast cancer cells are taken from refs. [10] and [19], respectively. Centre lines and box limits represent average values and error bars (s.e.m.), respectively. All errors were calculated from the errors of the data presented in Fig. 3. For the range of theoretical strain estimates deduced from the constriction geometries see 'Alternative strain measures' section in the Supplementary Information. χ^2 values are based on the residuals of the fitted data sets, and model fit parameters are presented in Tables 1 and 2, respectively.

Table 1 | χ^2 and *P* values of the fit of the experimental data to the predicted scaling laws of the two nucleation mechanisms

χ^2 (*P* value)	Bone cancer cells	Metastatic breast cancer cells	White blood cells
Heterogeneous nucleation	0.28 (>0.99)	2.29 (0.81)	21.19 (<0.01)
Homogeneous nucleation	113.94 (<0.01)	13.22 (0.02)	13.72 (<0.01)

If the measured scaling law is described by the nucleation mechanism, the sum of the residuals is expected to follow a χ^2 distribution where the number of degrees of freedom is equal to the number of fitted data points. In this context, $P=1$ signifies a perfect fit and $P=0$ means that the data do not fit the predicted scaling law. Due to the lack of reporting of s.e.m. values for the constriction dimensions in refs. [10,19], horizontal deviations of the strains for the metastatic breast cancer cells and the white blood cells could not be calculated and were not included in the *P* values calculation. The effect of such deviations on the fit is expected to significantly increase the *P* value of the fit of the metastatic breast cancer cell data to the homogeneous nucleation model, as is apparent from Fig. 4b; for this reason, the metastatic breast cancer cell data are considered to fit the homogeneous model based on visual observation rather than the *P* value.

with increasing ε. For small stresses, this decrease is expected to be approximately linear. In contrast, the energy barrier for homogeneous nucleation is the energy required to nucleate a critical hole in the lamina away from the BLasket[11]. This energy is inversely proportional to the lateral strain ε, which leads to the nucleation rate described by equation (1). However, as discussed in the 'Nuclear blebs and chromatin herniation' section in the Supplementary Information, applied strain can induce blebs that are not associated with lamina holes. To ascertain that the blebs we observe are associated with such holes and subsequent chromatin herniation (hallmark of lamina holes, see 'Nuclear blebs and chromatin herniation' in the Supplementary Information), we image the chromatin content in the blebs. This is done using cGAS, a cytoplasmic protein that binds chromatin when the NE ruptures, as we verified by a direct perturbation of the NE using atomic force microscopy (AFM) (Supplementary Fig. 3b).

The two different nucleation mechanisms also result in different predictions for the conditions under which each dominates. The mechanisms can be distinguished by their dependence on the density of the lamina molecules. The disassembly energy of the BLasket is an intrinsic property of its proteins; this is only indirectly affected by the lamina composition. In contrast, the energy required to nucleate a hole in the homogeneous region of the lamina directly increases with increasing density of the lamina; thus, increased expression of lamina proteins is expected to directly increase the energy barrier of homogeneous nucleation. For that reason, for low-density laminae, such as those found in cells comprising soft tissues[16,17], we predict that the homogeneous region of the lamina is the weakest link and homogeneous nucleation will dominate; for nuclei characterized by dense laminae, on the other hand, the BLasket is the weakest link and heterogeneous nucleation will dominate (see Supplementary Information).

It is important to note that equations (1) and (6) account for the rate of nucleation, that is, the probability of a lamina to nucleate a hole in a time interval of a single fluctuation, which is the Boltzmann factor derived from the appropriate energy barrier[18]. The post-migration, total fraction of blebbed nuclei ϕ, which we measure, depends on the migration time as well. However, the migration time only contributes an additive term to the logarithm of the theoretical nucleation probability $T(\phi) = \log(-\log(1-\phi))$, which is the sum of the logarithm of the probability for hole nucleation (in a single attempt) and the logarithm of the number of attempts (see 'Data fit' section). The former scales with the energy barrier of the dominant nucleation mechanism: nucleation due to BLasket disassembly is characterized by an approximately linear relation between $T(\phi)$ and the strain, with nonlinear corrections for high strains. In contrast, hole nucleation due to delocalized stretching of the homogeneous region of the lamina is characterized by a linear relation between $T(\phi)$ and the inverse of the strain.

To test the scaling prediction of these two different mechanisms, migration of non-metastatic bone cancer (U2OS, high lamina density[16]) cells through Transwell pores of different diameters (2–8 μm) was induced. Transwell pores are ideal for measurements of the scaling relation as the simple, very long, circular symmetry of the pore allows us to easily calculate the strain applied to the lamina as a

Table 2 | Heterogeneous and homogeneous nucleation model fit parameters of the bone cancer, metastatic breast cancer and white blood cells

	Bone cancer cells	Metastatic breast cancer cells	White blood cells
Disassembly radius[a], R_d	63.6 ± 2 nm	79.5 ± 3.1 nm	37.1 ± 2.8 nm
Spring constant[a], α	$(1.6 \pm 0.43) \times 10^{-2} \frac{k_B T}{nm^2}$	$(3.6 \pm 8.2 \times 10^{-26}) \times 10^{-12} \frac{k_B T}{nm^2}$	$(5.7 \pm 2.2 \times 10^{-34}) \times 10^{-15} \frac{k_B T}{nm^2}$
Disassembly strain[a], ε_d	1.12 ± 0.32	$(8.4 \pm 0.6) \times 10^{-10}$	<0
Line tension[b], γ	$(9 \pm 0.3) \times 10^{-3} \frac{k_B T}{nm}$	$(2 \pm 0.08) \times 10^{-2} \frac{k_B T}{nm}$	$(9 \pm 0.7) \times 10^{-3} \frac{k_B T}{nm}$

[a]Fit parameters of the heterogeneous model R_d and α and calculated disassembly strain ε_d (metastatic breast cancer and white blood cells are not biophysically reasonable); [b]line tension as a fit parameter of the homogeneous model.

function of the pore radius (see 'Strain estimates in the experimental geometry' section). Following migration, the cells were fixed, stained and imaged and the fractions of blebbed nuclei were measured; the data for different strains were then fit to the two nucleation models. To ascertain that the blebs are formed due to lamina hole nucleation, we repeated the migration experiment with bone cancer cells transfected with cGAS. More than 95% of the blebs in cells over-expressing cGAS were found to contain cGAS within the bleb (Supplementary Fig. 3a), indicating chromatin herniation due to lamina holes (see 'Nuclear blebs and chromatin herniation' section in the Supplementary Information) as well as previous NE rupture in the blebs.

In addition, to compare the mechanisms relevant to nuclei with lower laminae density, we also fit previously published data for bleb formation caused by migration through constrictions of white blood cells (hDC)[10] and metastatic breast cancer cells (MDA-MB-231)[19]; both of these cell types have lower lamina densities than bone cancer cells[16]. In contrast to our measurements of the fraction of nuclei that show blebs, the data from refs. [10,19] are based on observations of nucleoplasmic proteins leakage, a hallmark of NE rupture rather than of blebbing. However, in the majority of the NE ruptures of the metastatic breast cancer cells, bleb formation preceded or coincided with NE rupture[19]. Moreover, almost all blebs in the metastatic breast cancer cells formed at lamina sites of sparse or absent lamin B1 network, suggesting that these blebs are most probably due to lamina holes. This implies, at least for the bone and breast cancer cell lines, that blebbing due to lamina hole nucleation and the observation of NE rupture are equivalent. In contrast, this might not be true for white blood cells, in which chromatin-less blebs (supplementary fig. 4a of ref. [10]), chromatin herniation and NE rupture without visible formation of blebs (supplementary video 2 of ref. [10]) have all been reported; thus, the data for the white blood cells cannot be exclusively interpreted as representing lamina hole nucleation and may also include blebs formed by detachment of the NE from the lamina. The difference between the white blood cells and the metastatic breast cancer cells may be explained by the different geometries of the constrictions used in refs. [10,19]. The constrictions used in ref. [19] do not induce high, positive curvatures for the prolonged duration of the migration; thus, it is unlikely that they can induce bleb formation by NE detachment. In contrast, the rectangular constrictions of ref. [10] may induce the high curvature that promotes NE detachment, and not blebs due to lamina hole nucleation and chromatin herniation (see 'Nuclear blebs and chromatin herniation' in the Supplementary Information). Moreover, the long and narrow geometry of these constrictions may prevent visible bleb growth while the leading edge is within the constriction, which might explain the observation of blebless NE rupture in ref. [10] and not in ref. [19].

Our data for bone cancer cells show a poor fit to the scaling prediction for homogeneous nucleation, but a good fit to the heterogeneous nucleation model (Table 1 and Fig. 4), with values of fit parameters that are within the biologically reasonable range (Table 2); for a detailed discussion regarding ε_d, see Supplementary Information. The model parameters obtained from the fit of the metastatic breast cancer data to the heterogeneous model (Table 2) are not biophysically significant; the value of α in Table 2 is very small, implying unstable BLaskets (see 'Data fit' section). In contrast, the fit of the metastatic breast cancer cells data to the homogeneous model is good (Fig. 4b); this statement is based on visual observation of Fig. 4b rather than the χ^2 value, because the latter does not account for the uncertainty in the lateral strain due to an unknown error or strain estimation scheme (see Supplementary Information). We therefore conclude that lamina hole formation in breast cancer cells is best described by the homogeneous nucleation mechanism. The white blood cell data show a reasonable fit to the homogeneous mechanism (Table 1), but a biophysically meaningless fit to the heterogeneous model, because it results in $R_d < R_N$ and very small value of α (Table 2). However, the fit of the white blood cells data to the homogeneous mechanism is of lower quality compared with that of the metastatic breast cancer cells (Fig. 4b, inset). Given the observations of chromatin-less blebs (supplementary fig. 4a of ref. [10]), the low-quality fit might be caused by the presence of additional NE ruptures preceded by NE detachment from the lamina, which is outside the scope of our theory. Accordingly, the white blood cell data cannot be considered as exclusively representing lamina hole nucleation.

The results for the bone and breast cancer cells are in line with our qualitative predictions that relate lamina density to the relative prevalence of the type of nucleation: homogeneous nucleation due to stretching of the lamina is the dominant mechanism in low-density laminae (such as in metastatic breast cancer) while heterogeneous nucleation, possibly due to nuclear basket disassembly, dominates in high-density laminae (as in bone cancer cells). Future experiments in a single cell type with modifications that control lamina density and/or nuclear pore/basket stability can further test our predictions.

The physical model presented in this Article focuses on the nucleation of lamina holes, an important problem in biology, which, as we also show, is a necessary first step in the loss of NE integrity and resulting chromatin and genetic changes. However, our theory is more general and can be used, for example, as a starting point for analysis of the nucleation of cortical holes and associated cellular blebs[20] as well as holes in bacteria membrane by antimicrobial peptides, molecules that form channels in the plasma membranes of bacteria and lead to their lysis (death)[21]. Furthermore, the research presented here demonstrates how even generic information that relates the structure and properties of impurities in a system can be used to quantitatively analyse heterogeneous nucleation in phase transitions.

Online content

Any methods, additional references, Nature Research reporting summaries, source data, statements of code and data availability and associated accession codes are available at https://doi.org/10.1038/s41567-019-0506-8.

Received: 15 June 2018; Accepted: 15 March 2019;
Published online: 06 May 2019

References

1. Binder, K. Theory of first-order phase transitions. *Rep. Prog. Phys.* **50**, 783–859 (1987).
2. Oxtoby, D. W. Nucleation of first-order phase transitions. *Acc. Chem. Res.* **31**, 91–97 (1998).
3. Schlögl, F. Chemical reaction models for non-equilibrium phase transitions. *Z. Phys.* **253**, 147–161 (1972).
4. Shah, P., Wolf, K. & Lammerding, J. Bursting the bubble–nuclear envelope rupture as a path to genomic instability? *Trends Cell Biol.* **27**, 546–555 (2017).
5. Irianto, J. et al. DNA damage follows repair factor depletion and portends genome variation in cancer cells after pore migration. *Curr. Biol.* **27**, 210–223 (2017).
6. Newport, J. W. & Forbes, D. J. The nucleus: structure, function and dynamics. *Annu. Rev. Biochem.* **56**, 535–565 (1987).
7. Hatch, E. M. & Hetzer, M. W. Nuclear envelope rupture is induced by actin-based nucleus confinement. *J Cell Biol.* **215**, 27–36 (2016).
8. Deviri, D., Discher, D. E. & Safran, S. A. Rupture dynamics and chromatin herniation in deformed nuclei. *Biophys. J.* **113**, 1060–1071 (2017).
9. Irianto, J. et al. Constricted cell migration causes nuclear lamina damage, DNA breaks and squeeze-out of repair factors. Preprint at http://biorxiv.org/content/early/2015/12/30/035626 (2015).
10. Raab, M. et al. ESCRT III repairs nuclear envelope ruptures during cell migration to limit DNA damage and cell death. *Science* **352**, 359–362 (2016).
11. Idiart, M. A. & Levin, Y. Rupture of a liposomal vesicle. *Phys. Rev. E* **69**, 061922 (2004).
12. Chabanon, M., Ho, J. C., Liedberg, B., Parikh, A. N. & Rangamani, P. Pulsatile lipid vesicles under osmotic stress. *Biophys. J.* **112**, 1682–1691 (2017).
13. Pollak, E. Theory of activated rate processes: a new derivation of Kramers' expression. *J. Chem. Phys.* **85**, 865–867 (1986).
14. Knockenhauer, K. E. & Schwartz, T. U. The nuclear pore complex as a flexible and dynamic gate. *Cell* **164**, 1162–1171 (2016).
15. Sens, P. & Safran, S. Pore formation and area exchange in tense membranes. *Europhys. Lett.* **43**, 95–100 (1998).
16. Swift, J. et al. Nuclear lamin-A scales with tissue stiffness and enhances matrix-directed differentiation. *Science* **341**, 975 (2013).
17. Buxboim, A. et al. Matrix elasticity regulates lamin-A,C phosphorylation and turnover with feedback to actomyosin. *Curr. Biol.* **24**, 1909–1917 (2014).
18. Hänggi, P., Talkner, P. & Borkovec, M. Reaction-rate theory: fifty years after kramers. *Rev. Mod. Phys.* **62**, 251–342 (1990).
19. Denais, C. M. et al. Nuclear envelope rupture and repair during cancer cell migration. *Science* **352**, 353–358 (2016).
20. Charras, G. & Paluch, E. Blebs lead the way: how to migrate without lamellipodia. *Nat. Rev. Mol. Cell Biol.* **9**, 730–736 (2008).
21. Brogden, K. A. Antimicrobial peptides: pore formers or metabolic inhibitors in bacteria? *Nat. Rev. Microbiol.* **3**, 238–250 (2005).
22. Schooley, A., Vollmer, B. & Antonin, W. Building a nuclear envelope at the end of mitosis: coordinating membrane reorganization, nuclear pore complex assembly and chromatin de-condensation. *Chromosoma* **121**, 539–554 (2012).
23. Azimi, M. & Mofrad, M. R. Higher nucleoporin-importin β affinity at the nuclear basket increases nucleocytoplasmic import. *PloS One* **8**, e81741 (2013).
24. Goodsell, D. & Markosian, C. Molecule of the month: Nuclear pore complex. *PDB* https://doi.org/10.2210/rcsb_pdb/mom_2017_1 (2017).

Acknowledgements

The authors thank E. Bairy, O. Cohen, M. Elbaum, M. King, J. Lammerding, D. Lorber, A. Moriel, S. Nandi, V. Shenoy and K. Wolf for useful comments, and M. Piel for valuable discussions, including about the volume loss of highly deformed nuclei. The authors also thank K. Pannell and E.J. Chen (undergraduates from Rice University and New York University, respectively) for valuable support in the pore etching experiments. The research was supported by Human Frontiers Sciences Program grant RGP0024, National Institutes of Health/National Cancer Institute PSOC award U54 CA193417, National Heart Lung and Blood Institute awards R01 HL124106 and R21 HL128187, NIH fellowship F32 CA228285, the US–Israel Binational Science Foundation, the Israel Science Foundation, a grant from the Katz–Krenter Foundations, a National Science Foundation Materials Science and Engineering Center grant to the University of Pennsylvania, as well as continuing support from the Villalon and Perlman Family Foundations. The content of this article is solely the responsibility of the authors and does not necessarily represent the official views of the National Institutes of Health or other granting agencies.

Author contributions

C.R.P. and D.E.D. designed the experiments. D.D. and S.A.S. developed the theory. C.R.P., L.J.D. and I.L.I. performed the experiments and D.E.D. assisted with analysis. D.D. and S.A.S. wrote the paper with important contributions from C.R.P. and D.E.D.

Additional information

Supplementary information is available for this paper at https://doi.org/10.1038/s41567-019-0506-8.

Reprints and permissions information is available at www.nature.com/reprints.

Correspondence and requests for materials should be addressed to D.D.

Publisher's note: Springer Nature remains neutral with regard to jurisdictional claims in published maps and institutional affiliations.

Methods

Experimental methods. *Cell culture.* U2OS human osteosarcoma cells were cultured in DMEM high-glucose medium (Gibco, Life Technologies), supplemented with 10% fetal bovine serum (FBS, MilliporeSigma) and 1% penicillin/streptomycin (MilliporeSigma).

Transfection. GFP-LBR was a gift from R.-H. Chen (Academia Sinica) and mCherry-cGAS was a gift from R. Greenberg (University of Pennsylvania)[25]. We transfected either GFP-LBR or mCherry-cGAS (0.5 ng ml^{-1}) with 1 g ml^{-1} Lipofectamine 2000 (Invitrogen, Life Technologies) for 24 h in DMEM high-glucose medium (Gibco, Life Technologies), supplemented with 10% FBS.

Pore etching. To generate a denser data set for pore migration studies, commercial microporous membrane filters were chemically etched to increase the pore diameter. Transwell polycarbonate membranes are commercially available with 3, 5 and 8 µm pore diameters. Membranes with an initial pore diameter of 3 µm (Corning 3415) were etched with 2 M NaOH in a 60 °C incubator for 72 min and 120 min to generate 4-µm- and 5-µm-diameter pores, respectively. The same conditions were used to etch membranes with an initial pore diameter of 5 µm (Corning 3421) to generate 6-µm- and 7-µm-diameter pores. NaOH concentration and etching times were adapted from ref. [26]. Falcon insert polyester membranes are commercially available with 1 and 3 µm pore diameters. Etching these membranes under the same conditions as the Transwell membranes frequently led to tearing that extended to the edge where the membrane was adhered to the polystyrene housing. So, instead, membranes with an initial pore diameter of 1 µm (Corning 353104) were first irradiated with 365 nm ultraviolet light (Spectroline XX-15A, 0.7A) for 30 min per side and then etched with 9 M NaOH at room temperature (22 °C). Etching for 4.5 h and 5 h generated 2.2-µm- and 2.3-µm-diameter pores, respectively. Following etching, membranes were washed extensively with MilliQ water and dried under vacuum. Etched pores were characterized by confocal microscopy and scanning electron microscopy (Supplementary Fig. 4). The etching process was also expected to decrease the membrane thickness, which was confirmed by confocal microscopy. Membranes were sterilized with ultraviolet irradiation before constricted migration experiments. For scanning electron microscopy (SEM), membranes were cut from polystyrene housing and adhered to an SEM sample peg with double-sided carbon tape. The electron microscope (FEI Quanta 600 FEG Mark II ESEM) was operated in wet environment mode.

Transwell migration. Migration assays were performed using commercially available Transwell polycarbonate membranes with pore diameters of 3, 5 and 8 µm as well as etched membranes (see above) with modified pore diameters of 4, 5, 6 and 7 µm. Detached U2OS cells were seeded on top of each membrane at a density of 300,000 cells cm^{-2}; supplemented medium was added to the top and bottom of the membrane so that there was no nutrient gradient. Cells were allowed to migrate to the bottom over the course of 24 h at 37 °C and 5% CO_2. Finally, membranes—with un-migrated cells attached on top and migrated cells attached on the bottom—were formaldehyde-fixed and stained as described in the next section.

Immunostaining and imaging. Cells were fixed in 4% formaldehyde (MilliporeSigma) for 15 min, and then permeabilized by 0.25% Triton-X (MilliporeSigma) for 10 min. After 30 min blocking by 5% bovine serum albumin (BSA, MilliporeSigma), cells were incubated in primary antibodies overnight at 4 °C. The antibodies used include anti-lamin-A/C (Santa Cruz and Cell Signaling), anti-lamin-B (Santa Cruz), anti-lamin-B1 (Abcam) and mAB414 against nuclear pore complex proteins (Abcam). Finally, following a 90 min incubation in secondary antibodies (Thermo Fisher), cells were stained with 8 µM Hoechst 33342 (Thermo Fisher) for 15 min, and then mounted on #1.5 coverslips using Prolong Gold antifade reagent (Invitrogen, Life Technologies). Unless otherwise specified, steps were carried out at room temperature. Confocal imaging of cells was done on a Leica TCS SP8 system with a ×63/1.4 NA oil-immersion objective. SEM of commercially available and etched Transwell membranes was performed with an FEI Quanta 600 FEG Mark II ESEM, operated in wet environment mode. Images were quantified in ImageJ[27].

Identification of nuclear blebs. Nuclear blebs are characterized by enrichment of lamin A and near absence of lamin B, as described previously for multiple cell lines including U2OS[5]. To detect blebs in a given confocal projection, the lamin A fluorescence signal (red) is superimposed over the lamin B fluorescence signal (green) such that nuclear regions of high lamin A/low lamin B (that is, high red/low green) are easily detected by eye (Fig. 2; for more examples see Supplementary Fig. 5). Many blebs present as irregular protrusions from the nucleus and are thus highly conspicuous; others present as subtler ‘ scars’ in the nuclear body. Nuclei are classified as either bleb-positive or bleb-negative, and then the fraction of blebbed nuclei is calculated.

Nuclear indentation by AFM during fluorescent imaging. U2OS cells transfected with GFP-LBR and mCherry-cGAS, as described above, were re-plated on glass coverslips at a density of 60,000 cells cm^{-2} and cultured overnight. Coverslips were then mounted in the fluid cell of a hybrid AFM system (MFP-3D-BIO; software, MFP-3D + Igor Pro 6.05; Asylum Research, Oxford Instruments), which was integrated with an inverted optical fluorescence microscope (Olympus IX81 with ×40/0.60 NA objective). The fluid cell was maintained at ~29 °C and filled with DMEM high-glucose medium (Gibco, Life Technologies), supplemented with 10% FBS, buffered at pH 7.4 with 25 mM Hepes to prevent cell death[28]. Nuclei were indented using MSCT-AUHW (Bruker) cantilevers with a nominal spring constant of 0.03 N m^{-1}, a nominal tip radius of 10–40 nm and a nominal tip height of 2.5–8 µm. The thermal fluctuations method was used to calibrate the cantilever spring constant before experiments. Experiments were carried out as described in ref. [29]: the cantilever locally compressed the nucleus with forces of ~10–30 nN until the cantilever deflection reached a predefined value, at which point the probe was held steady for 100 s. Before, during and after indentation, fluorescent images were captured every ~10–15 s. Over dozens of experiments, mCherry-cGAS reliably accumulated in the nucleus at the site of indentation.

Theoretical methods. *Strain estimates in the experimental geometries.* We used geometrical arguments to estimate the strain dependence of experimental measurements of the bleb formation probability as observed in assays with three different types of constriction geometry: (C) Circular, Transwell pores, (R) nano-fabricated rectangular channels (supplementary fig. 6 in ref. [10]) and (X) nano-fabricated, juxtaposed pillars with a more complex geometry (see supplementary fig. 1a in ref. [19]). Motivated by observations that the nucleus can sustain pressure gradients over timescales comparable to those of migration[30], we assumed that the nuclear volume is conserved during migration. For each geometry, we calculated the shape and area of a constricted nucleus that preserve its volume (relative to the unconstricted nucleus) while minimizing its surface area (and hence surface energy). Because migration timescales are of the order of tens of minutes[10,19], which is an order of magnitude longer than the typical viscoelastic timescales of the lamina (estimated to be tens of seconds[8]), we considered the strain in the lamina to be uniform. The constriction-induced flows thus equilibrate the strains[31] on timescales associated with the migration. Therefore, the strains of the lamina were simply estimated as the difference between the deformed and undeformed surface areas, divided by the undeformed surface area.

Current experiments do not accurately measure the deformed shape of the nuclei and hence we cannot precisely know their deformed area. Thus, we considered several different strain measures based on the known geometries of the different types of constriction used in the experiments. The shape of the deformed nuclei was estimated by minimization of the nucleus area under geometrical constraints imposed by the constriction. Alternative, simpler strain measures, which weigh the geometrical characteristics of the constrictions differently, are presented in the Supplementary Information: these support the robustness of the results presented in Fig. 4. For the circular geometries (type C) applicable to the new measurements presented here, the shape of the nuclei was approximated as a spheroid with two of its axes lengths equal to the constriction radius and the third determined by volume conservation. This choice of a spheroidal shape for nuclei migrating through a circular constriction is supported by recent experimental observations[32]. Similarly, the shape of the nuclei in rectangular constrictions (type R, as used in ref. [10]) was approximated as an ellipsoid with the (in general, different) lengths of two of its axes fixed by the dimensions of the rectangular constriction, and the third determined by volume conservation. Although rectangular constrictions are different from circular ones due to the presence of sharp corners, a sharply cusped nuclear shape is energetically improbable due to divergence of the lamina and NE bending energies at infinitely sharp cusps. The bending energy thus gives rise to a smoothing of the shape at small length scales[33] but is negligible compared with the surface tension at long length scales[34]. We therefore expect the shape of nuclei migrating through rectangular constrictions to be ellipsoidal as well. In contrast to constriction geometries of type (C) and (R), constrictions of type (X) (see Supplementary Fig. 1) are very complex; in that case, it is very difficult to calculate the nuclear shape as an analytical solution to an optimization problem. Thus, we approximated the shape from images of the constricted nuclei, which show that the nuclei follow the contour of the pillars and then form approximately circular segments at their other ends[19]. For detailed explanations and the expressions that were used to estimate the strains, see Supplementary Information.

Data fit. The scaling relations, equations (1) and (6), predict the strain dependence of the probability P for the nucleation of lamina holes. These are expressions for the probabilities of nucleation for a single attempt (fluctuation) at a single nucleation site—a homogeneous lamina region or a BLasket, respectively, for the homogeneous and heterogeneous mechanisms. During migration of a cell through a constriction, the nucleus may experience multiple attempts at hole nucleation in the lamina, either at the same sites at different times during the transit, or at different sites within the lamina; we denote the number of possible nucleation sites as N, the transit time as T_m and the average time between nucleation attempts at a single site by τ. We begin here with a detailed theoretical analysis that relates the observable measured in our experiments and in refs. [10,19]—the fraction of nuclei ϕ that exhibit blebbing or NE rupture—to the probability P for nucleation of a lamina hole at a single site and with a single attempt.

We denote the probability of nucleation of a hole at a single site, during the entire transit time T_m, by P_{site}; this probability is assumed to be the same for all sites due to the uniformity of the lamina stress and strain (at long times; see section 'Strain estimates in the experimental geometries'). The fraction ϕ is equivalent to the probability for at least one successful nucleation event at any site within the lamina during the entire transit time. Conversely, its complement $1-\phi$ is the probability that no hole will nucleate at any of the lamina sites. The probability of a site remaining intact during the entire transit is $1-P_{site}$, so the probability $1-\phi$ of all N uncorrelated sites to stay intact during the transit is related to P_{site} by the relation $1-\phi=(1-P_{site})^N$. Motivated by the large number of nuclear pore complexes (of the order of 2,000 in vertebrates[35]) and the even larger number of homogeneous nucleation sites in the lamina, we assume that the number of possible nucleation sites for either mechanism is very large, $N\gg 1$. In that scenario, the definition of the exponential function as a limit can be used to approximate $(1-P_{site})^N \approx e^{-NP_{site}}$, so that

$$1-\phi = e^{-NP_{site}} \tag{7}$$

If P_{site} is much larger than $1/N$, then equation (7) shows that the overall nucleation fraction ϕ is almost unity. This is not the case for the fitted data points of Fig. 4, so we conclude that in our experiments NP_{site} is of order unity or smaller.

In the case of multiple, uncorrelated BLaskets, the probability for a nucleation in a single attempt in each BLasket is the same as we derived in our theory for a single BLasket (see Supplementary Information). This is also true for the case of homogeneous nucleation, in which the probability of nucleation at a specific site is determined by the lateral stress, which is taken to be uniform across the lamina (see section 'Strain estimates in the experimental geometries'). Therefore, in general, the probability P_{site} is determined by a function of the predicted probability P for a single attempt at hole nucleation at a single site, and the average number of attempts, T_m/τ. We now show that in the two limiting cases of interest, $P_{site}\approx(T_m/\tau)P$.

A powerful assumption that is commonly used in statistical mechanics is that fluctuations that give rise to nucleation are uncorrelated in time[36]. In this case, the probability $g(k)$ of having k attempts in a time T_m obeys a Poisson distribution:

$$g(k)=\frac{1}{k!}e^{-\frac{T_m}{\tau}}\left(\frac{T_m}{\tau}\right)^k \tag{8}$$

We note that the value of the average time between fluctuations τ may span a wide range, depending on the molecular details of an attempt (see Supplementary Information). This motivates us to consider two asymptotic limits. The first limit is where the transit time T_m is much larger than the average time between attempts, τ. In this limit, every nucleation site experiences an average of $\sum_k k\cdot g(k)=T_m/\tau\gg 1$ nucleation attempts during the transit. The relation between the total probability P_{site} per site and the probability per attempt P is similar to equation (7); thus $P_{site}=1-\exp(-(T_m/\tau)P)$. Because in our measurements $P_{site}\ll 1$, then $(T_m/\tau)P$ is also, so the approximation $P_{site}\approx(T_m/\tau)P$ is valid. The second limit we consider is the one where the transit time is smaller than the average time between fluctuations $T_m\ll\tau$ so that the effect of multiple nucleation attempts is negligible. In that case, the probability of even one event can be calculated using equation (8) as $1-g(0)=1-\exp(-T_m/\tau)\approx T_m/\tau$. The probability P_{site} in that case is the product of the probability that even one event will occur and the probability P that this attempt will lead to successful nucleation, that is, $P_{site}\approx(T_m/\tau)P$. In conclusion, we find that the two asymptotic limits of $T_m\ll\tau$ and $T_m\gg\tau$ both result in the same approximate expression $P_{site}\approx(T_m/\tau)P$. We thus use $P_{site}\approx(T_m/\tau)P$ for any value τ in our experimental analysis. Substitution of the expression for P_{site} into equation (7), followed by reordering, leads to our final relation, used to fit the data:

$$1-\phi=e^{-\frac{NT_m}{\tau}P} \tag{9}$$

The probability $P(\varepsilon)$ is mechanism-specific and is exponential in the nucleation energy barrier of the appropriate mechanism[13]: it is given by equation (1) for homogeneous nucleation and by equation (6) for heterogeneous nucleation. Therefore, $T(\phi)=\log(-\log(1-\phi))$ (where ϕ is the observed fraction of nuclei presenting blebbing or NE rupture) results in the sum of the logarithm of the theoretical, strain-dependent nucleation probability P and a constant $\log(NT_m/\tau)$ that is independent of the strain ε. Because the two mechanisms predict different strain dependence, the scaling of $T(\phi)$ with the strain can distinguish between homogeneous and heterogeneous nucleation. For the homogeneous mechanism, $T(\phi)$ scales linearly with the inverse of the strain, while for the heterogeneous mechanism, $T(\phi)$ scales linearly with the strain ε, with nonlinear corrections for large strains.

The scaling relation we predict for the strain dependence of the heterogeneous nucleation mechanism (in the relatively high strain regime, as given by equation (6)) depends on two parameters, which are a priori unknown: the BLasket disassembly radius R_d and its phenomenological 'spring constant' α that characterizes the BLasket deformability. This situation is different from the scaling relation of the homogeneous nucleation mechanism (as given by equation (1)), which depends on a single parameter, the square of the line tension divided by the 2D elastic modulus γ^2/E. Although a two-parameter model can be more easily fit to the data, we avoid that temptation by considering an additional condition that helps distinguish between fits that are statistically significant (according to a χ^2 test applied to the distribution of the sum of the residuals of the fitted data points) but result in biologically unreasonable values of the fit parameters and those that are biologically meaningful: we demand that the fitted values of the parameter α be within a reasonable range of $\alpha/E\sim 1-20$, estimated from independent experiments[16,37], in which NPCs in the nuclei of cells grown on substrates of different stiffnesses were imaged; the range of α/E is estimated from our model and the observed degree of expansion of the NPC on the stiff substrates. The invalidity of the asymptotic limits of the values of α can be intuitively understood as follows. Extremely small values of $\alpha\ll 1$ imply extremely soft BLaskets that can easily disassemble under thermal fluctuations and would not be stable even in undeformed lamina, as described by the energy barrier given by equation (5). This contradicts the observed stability of the cell nucleus. On the other hand, extremely large values of $\alpha\gg 1$ imply stiff BLaskets that hardly change their size or disassemble, as described by the energy barrier in equation (5). This suggests that BLasket nucleation is highly improbable, so the vast majority of the lamina holes would nucleate at the homogeneous region of the lamina rather than the BLaskets, which is not consistent with the fit to the heterogeneous nucleation model itself. We compare the biophysically relevant range of α to its value obtained from the fits of the data for the logarithm of the theoretical nucleation probability $T(\phi)$ as a function of strain, predicted by the high strain regime of equation (6) using the Mathematica command NonLinearModelFit (Fig. 4); the fit of the white blood cells and metastatic breast cancer cells resulted in unphysical, negative values of α or R_d, so we constrained the allowed range to have positive α and R_d for these cells. Data fits that are statistically significant and yield reasonable values α are considered to be good fits to the heterogeneous nucleation mechanism. In accordance with the measurements of the elastic modulus in fig. 7D of ref. [16], the elastic modulus of the lamina of stiff nuclei (that is, in bone cancer cells) was estimated as 0.2 kPa and of the softer nuclei (metastatic breast cancer and white blood cells) as 0.1 kPa; the elastic moduli were converted to 2D area expansion moduli by multiplication with the lamina thickness (~15 nm; ref. [38]). Motivated by experimental evidence for NPCs, we took the equilibrium BLasket radius in the absence of any external deformations to be 50 nm (refs. [14,39,40]). In the absence of evidence for active noise in the lamina, we chose the value of the noise parameter β^{-1} to be k_BT to account for purely thermal noise.

Reporting Summary. Further information on research design is available in the Nature Research Reporting Summary linked to this article.

Data availability

Raw data points are plotted in Fig. 3 and are available in other formats from the corresponding author on request.

Code availability

The code that was used to fit the experimental data to the scaling prediction of the heterogeneous nucleation mechanism, and the code that was used to estimate the strain in constrictions of type (3) geometry, are available from the corresponding author on request.

References

25. Harding, S. M. et al. Mitotic progression following DNA damage enables pattern recognition within micronuclei. *Nature* **548**, 466–470 (2017).
26. Cornelius, T. et al. Investigation of nanopore evolution in ion track-etched polycarbonate membranes. *Nucl. Instrum. Methods Phys. Res. B* **265**, 553–557 (2007).
27. Schneider, C. A., Rasband, W. S. & Eliceiri, K. W. NIH image to ImageJ: 25 years of image analysis. *Nat. Methods* **9**, 671–675 (2012).
28. Frigault, M. M., Lacoste, J., Swift, J. L. & Brown, C. M. Live-cell microscopy—tips and tools. *J. Cell Sci.* **122**, 753–767 (2009).
29. Xia, Y. et al. Nuclear rupture at sites of high curvature compromises retention of DNA repair factors. *J. Cell Biol.* **217**, 3796–3808 (2018).
30. Petrie, R. J., Koo, H. & Yamada, K. M. Generation of compartmentalized pressure by a nuclear piston governs cell motility in a 3D matrix. *Science* **345**, 1062–1065 (2014).
31. Oron, A., Davis, S. H. & Bankoff, S. G. Long-scale evolution of thin liquid films. *Rev. Mod. Phys.* **69**, 931–980 (1997).
32. Buxboim, A. et al. Coordinated increase of nuclear tension and lamin-A with matrix stiffness outcompetes lamin-B receptor that favors soft tissue phenotypes. *Mol. Biol. Cell* **28**, 3333–3348 (2017).
33. Seifert, U. & Lipowsky, R. Adhesion of vesicles. *Phys. Rev. A* **42**, 4768–4771 (1990).
34. Safran, S. *Statistical Thermodynamics of Surfaces, Interfaces and Membranes* (CRC Press, 2018).
35. Adam, S. A. The nuclear pore complex. *Genome Biol.* **2**, reviews0007 (2001).

36. Reif, F. *Fundamentals of Statistical and Thermal Physics* (Waveland Press, 2009).
37. Elosegui-Artola, A. et al. Force triggers YAP nuclear entry by regulating transport across nuclear pores. *Cell* **171**, 1397–1410 (2017).
38. Turgay, Y. et al. The molecular architecture of lamins in somatic cells. *Nature* **543**, 261–264 (2017).
39. Hayama, R., Rout, M. P. & Fernandez-Martinez, J. The nuclear pore complex core scaffold and permeability barrier: variations of a common theme. *Curr. Opin. Cell Biol.* **46**, 110–118 (2017).
40. Upla, P. et al. Molecular architecture of the major membrane ring component of the nuclear pore complex. *Structure* **25**, 434–445 (2017).

nature research

Corresponding author(s): Dan Deviri

Last updated by author(s): Mar 13, 2019

Reporting Summary

Nature Research wishes to improve the reproducibility of the work that we publish. This form provides structure for consistency and transparency in reporting. For further information on Nature Research policies, see Authors & Referees and the Editorial Policy Checklist.

Statistics

For all statistical analyses, confirm that the following items are present in the figure legend, table legend, main text, or Methods section.

n/a	Confirmed	
☐	☒	The exact sample size (*n*) for each experimental group/condition, given as a discrete number and unit of measurement
☐	☒	A statement on whether measurements were taken from distinct samples or whether the same sample was measured repeatedly
☐	☒	The statistical test(s) used AND whether they are one- or two-sided *Only common tests should be described solely by name; describe more complex techniques in the Methods section.*
☐	☒	A description of all covariates tested
☐	☒	A description of any assumptions or corrections, such as tests of normality and adjustment for multiple comparisons
☐	☒	A full description of the statistical parameters including central tendency (e.g. means) or other basic estimates (e.g. regression coefficient) AND variation (e.g. standard deviation) or associated estimates of uncertainty (e.g. confidence intervals)
☐	☒	For null hypothesis testing, the test statistic (e.g. *F*, *t*, *r*) with confidence intervals, effect sizes, degrees of freedom and *P* value noted *Give P values as exact values whenever suitable.*
☒	☐	For Bayesian analysis, information on the choice of priors and Markov chain Monte Carlo settings
☒	☐	For hierarchical and complex designs, identification of the appropriate level for tests and full reporting of outcomes
☒	☐	Estimates of effect sizes (e.g. Cohen's *d*, Pearson's *r*), indicating how they were calculated

Our web collection on statistics for biologists contains articles on many of the points above.

Software and code

Policy information about availability of computer code

Data collection	Leica Application Suite X (LAS X) is the software platform for the Leica TCS SP8 microscope that we used to do confocal imaging. Our AFM system runs Igor Pro software (version 6.05) from WaveMetrics. Image analysis was performed using ImageJ via FIJI.
Data analysis	Figures were generated by Microsoft excel version 15.30 and by Python 2.7 via Spyder 3.2.4, Wolfram Mathematica version 10.0.0.0 was used to fit the experimental data to predicted scaling laws and to estimate lateral strains for the different constriction geometries.

For manuscripts utilizing custom algorithms or software that are central to the research but not yet described in published literature, software must be made available to editors/reviewers. We strongly encourage code deposition in a community repository (e.g. GitHub). See the Nature Research guidelines for submitting code & software for further information.

Data

Policy information about availability of data

All manuscripts must include a data availability statement. This statement should provide the following information, where applicable:

- Accession codes, unique identifiers, or web links for publicly available datasets
- A list of figures that have associated raw data
- A description of any restrictions on data availability

Raw data points are plotted in figure 3 and are available in other formats from the corresponding author on request.

Field-specific reporting

Please select the one below that is the best fit for your research. If you are not sure, read the appropriate sections before making your selection.

☒ Life sciences ☐ Behavioural & social sciences ☐ Ecological, evolutionary & environmental sciences

Life sciences study design

All studies must disclose on these points even when the disclosure is negative.

Sample size	For the experiments involving migration of U2OS cells through commercially available and custom-etched Transwell membrane pores, we used confidence interval calculations to roughly estimate appropriate sample sizes. For the 3 µm pore migration of U2OS cells transfected with mCherry-cGAS, included in the supplement, we analyzed ≥21 cells on both the top and bottom of the pore membrane (i.e. before and after migration). This sample size is sufficient to show that, in U2OS cells, the vast majority of nuclear blebs are positive for mCherry-cGAS, which indicates that these blebs contain chromatin herniates and thus originated by lamina hole formation. On the bottom of the pore membrane, we find that >95% of cells are cGAS-positive, so the margin of error in this case is ~9%. With a confidence level of 95%, the true cGAS-positive fraction is likely to be 86-100%, which, again, indicates that almost all U2OS nuclear blebs form due to lamina holes. For the AFM experiments, also included in the supplement, in which U2OS cells transfected with GFP-LBR and mCherry-cGAS were indented using cantilevers, we report data for 3 representative cells. We do not perform rigorous quantitation of these data or attempt to draw statistical conclusions; we simply show the consistent trend that lamina rupture (as indicated by loss of GFP-LBR) correlates spatiotemporally with nuclear entry/accumulation of mCherry-cGAS. A sample size of 3 cells is sufficient in this case because the three cells are representative of dozens of experiments, and they are used to illustrate general trends. Finally, we used a t-test to roughly estimate appropriate sample sizes for the supplemental 3 µm pore migration experiment in which U2OS cells were stained for lamin-A, lamin-B, and nuclear pore complex (NPC) proteins. We planned to measure the average intensities of DNA, lamin-A, lamin-B, and NPCs for: (1) nuclei without blebs, (2), the 'off bleb' regions of blebbed nuclei, and (3) the 'on bleb' regions of blebbed nuclei. For a power of 0.8, two-sided α of 0.05, normalized average DNA/protein intensity of 1.0 among nuclei without blebs, and common standard deviation of 0.2, a sample size of 28 is needed to detect an intensity difference of ≥15% between nuclei without blebs and the 'on bleb' or 'off bleb' regions of blebbed nuclei. With this sample size calculation as a rough guideline, we analyzed ≥30 cells per condition.
Data exclusions	No data were excluded from the study.
Replication	To verify the reproducibility of our experiments to measure fraction of blebbed nuclei after migration, we repeated these experiments for selected pore diameters: the 3, 5, and 8 µm pore assays (using commercially available pore membranes) were reproduced 3× each over a span of several months, and the 4, 5, and sub-3 µm etched-pore assays (using NaOH-etched membranes) were reproduced 2× each. As a percentage of the fraction of blebbed nuclei, the standard error of the mean (SEM) was found to be just 2%, 7%, and 17% for the repeated 3, 5, and 8 µm (commercial) pore assays, respectively. Furthermore, we conducted every assay in duplicate (i.e. two pore membranes per pore size). All of the bleb fractions reported in this study were measured by one experimenter (CRP), but to further verify the reproducibility of these results, two additional experimenters (Kalia Pannell and Emily J. Chen, see Acknowledgements) also independently quantified fraction of blebbed nuclei after migration through commercial 3 and 8 µm pores. All three experimenters obtained similar fractions (fractions differed by <10% and <30% for cells on the bottom of 3 and 8 µm pore membranes, respectively). To verify the reproducibility of our pore etching method, we imaged commercially available and etched pore membranes using either confocal or scanning electron microscopy, and then measured the pore diameters in ImageJ. For a given pore membrane, the distribution of pore sizes is very tight: for example, as a percentage of the mean, the standard deviation in pore diameter was found to be only ~6% for 5 µm pore membranes incubated in 2 M NaOH for 60, 90, or 120 minutes. Meanwhile, between membranes with nominally same-sized pores, the average pore size is statistically the same. AFM nuclear indentation experiments were repeated dozens of times; the 3 cells shown here are representative of these many replicates. The migration experiment involving U2OS cells transfected with mCherry-cGAS was conducted in duplicate; that is, two migration assays were performed simultaneously. Both assays yielded the same results: namely, that almost all U2OS nuclear blebs are positive for cGAS. The combined results from the two assays are reported here. Regarding the 3 µm pore migration experiment in which U2OS cells were stained for lamin-A, lamin-B, and NPC proteins: our DNA, lamin-A, and lamin-B intensity measurements are consistent with previous measurements from the Discher lab showing that nuclear blebs are deficient in lamin-B and DNA but abundant in lamin-A [Irianto et al. Curr Biol 2017].
Randomization	Random allocation of participants into experimental groups was not relevant to our study. All of our experiments were performed using the same bulk stock of U2OS human osteosarcoma cells. Published experiments involving other cell lines were carried out by other research groups.
Blinding	Blinding of investigators during data analysis was not feasible in our experiments to measure fraction of blebbed nuclei after migration. Since the rate of pore migration correlates strongly with pore size, the density of cells on the bottom of a Transwell membrane is a clear indicator of the pore diameter through which those cells migrated. For example, cells are very dense on the bottom of an 8 µm pore membrane but very sparse on the bottom of a sub-3 µm pore membrane. Therefore, it is not possible to conceal the pore diameter from an investigator who is counting blebbed nuclei in images of migrated cells on the membrane bottom. Blinding of investigators was not relevant to our AFM experiments because all cells belonged to the same experimental group: namely, U2OS cells, transfected with GFP-LBR and mCherry-cGAS, that showed lamina disruption and nuclear entry/accumulation of cGAS after indentation.

There were two experimental groups in our migration experiment involving U2OS cells transfected with mCherry-cGAS: cells that migrated to the bottom of the 3 µm pore membrane, and cells that remained unmigrated on top of the membrane. Cell density is much higher on the membrane top, so any investigator could distinguish top from bottom while analyzing images for cGAS entry into nuclear blebs. Blinding of investigators was thus not possible in this experiment.

In our investigation of NPC proteins, the analysis involved classifying nuclei according to whether or not they exhibited blebs--and, further, identifying the 'on bleb' and 'off bleb' regions of blebbed nuclei. Since the analysis itself required allocation of cells into experimental groups, blinding of investigators to group allocation was not relevant here.

Reporting for specific materials, systems and methods

We require information from authors about some types of materials, experimental systems and methods used in many studies. Here, indicate whether each material, system or method listed is relevant to your study. If you are not sure if a list item applies to your research, read the appropriate section before selecting a response.

Materials & experimental systems

n/a	Involved in the study
☐	☒ Antibodies
☐	☒ Eukaryotic cell lines
☒	☐ Palaeontology
☒	☐ Animals and other organisms
☒	☐ Human research participants
☒	☐ Clinical data

Methods

n/a	Involved in the study
☒	☐ ChIP-seq
☒	☐ Flow cytometry
☒	☐ MRI-based neuroimaging

Antibodies

Antibodies used

1. Cell Signaling α-lamin-A/C (4C11): 4777
2. Santa Cruz α-lamin-A/C (636): sc-7292, Lot #H1314
3. Santa Cruz α-lamin-B (M-20): sc-6217
4. Abcam α-lamin-B1: ab16048, Lot #GR3214420-1
5. Abcam mAB414 against nuclear pore complex proteins: ab24609, Lot #GR284387-11

Validation

The following validation statements, corresponding to the antibodies listed above, are reproduced from the manufacturers' websites:

1. "Lamin A/C (4C11) Mouse mAb detects endogenous levels of lamin A and lamin C proteins. It also reacts with the larger fragments of lamin A (50 kDa) and lamin C (41 kDa) produced by caspase cleavage during apoptosis. This antibody does not cross-react with lamins B1 and B2...Species Reactivity: Human, Mouse, Rat, Monkey."

2. "Lamin A/C (636) is recommended for detection of Lamin A and Lamin C of mouse, rat and human origin by Western Blotting (starting dilution 1:200, dilution range 1:100-1:1000), immunoprecipitation [1-2 µg per 100-500 µg of total protein (1 ml of cell lysate)], immunofluorescence (starting dilution 1:50, dilution range 1:50-1:500), immunohistochemistry (including paraffinembedded sections) (starting dilution 1:50, dilution range 1:50-1:500) and flow cytometry (1 µg per 1E06 cells)."

3. "Lamin B (M-20) is recommended for detection of Lamin B1 and, to a lesser extent, Lamin B2 of mouse, rat and human origin by Western Blotting (starting dilution 1:200, dilution range 1:100-1:1000), immunoprecipitation [1-2 µg per 100-500 µg of total protein (1 ml of cell lysate)], immunofluorescence (starting dilution 1:50, dilution range 1:50-1:500), immunohistochemistry (including paraffin-embedded sections) (starting dilution 1:50, dilution range 1:50-1:500), flow cytometry (1 µg per 1E06 cells) and solid phase ELISA (starting dilution 1:30, dilution range 1:30-1:3000)."

4. "Suitable for: ICC/IF, IHC-Fr, WB, IHC-P, IHC – Wholemount…Reacts with: Mouse, Rat, Human, Pig, Xenopus laevis, Indian muntjac."

5. "ab24609 reacts with Nuclear Pore Complex (NPC) Proteins. Aris et al (J. Cell Biol. 108:2059-2067, 1989). Suitable for: ChIP, WB, ICC/IF, IP, Electron Microscopy, IHC-Fr…Reacts with: Mouse, Rat, Cat, Human, Saccharomyces cerevisiae, Xenopus laevis, Caenorhabditis elegans, Drosophila melanogaster, Zebrafish."

Eukaryotic cell lines

Policy information about cell lines

Cell line source(s)

The U2OS human osteosarcoma cells used in our study were a gift from Dr. Roger Greenberg (University of Pennsylvania, Philadelphia, PA). The cells were originally purchased from ATCC.

Authentication

ATCC provides cell line authentication test recommendations per Tech Bulletin number 8 (TB-0111-00-02; year 2010). This bulletin recommends several types of tests for the authentication of cell lines. (1) Cell morphology check by microscopy, (2) growth curve analysis, and (3) mycoplasma detection by DNA staining (for filaments or extracellular particulates) were conducted within the last year on the U2OS cells used in this study. The cells maintained the expected morphology and

standard growth rates with no mycoplasma detected.

An additional ATCC-recommended authentication test was conducted on the U2OS cell line. (4) Identity verification via DNA was performed using single nucleotide polymorphism (SNP) arrays (SNPas). DNA was isolated from U2OS cells using the Blood and Cell Culture DNA Mini Kit (QIAGEN) per the manufacturer's instructions, and DNA samples were sent to the Center for Applied Genomics Core in The Children's Hospital of Philadelphia (Philadelphia, PA) for the SNPa HumanOmniExpress-24 Bead Chip Kit (Illumina), with >700,000 probes along the entire human genome. For each sample, the Genomics Core provided the data in the form of GenomeStudio files (Illumina). Chromosome copy number was analyzed in GenomeStudio with the cnvPartition plugin (Illumina). SNPa experiments also provided genotype data, which was used to give single nucleotide variant (SNV) data. Genotyping in this Illumina system relied on the correlation between total intensity and intensity ratio of the two probes, one for CG and another for AT. These correlations were mapped to a standard clustering file (Illumina) to give the SNP calls.

Consistent with ATCC's karyotype analysis, SNPa showed that the U2OS cells used in our study contain ~65 chromosomes, which agrees with altered chromosomes reported by ATCC. Moreover, genomic drift in terms of copy number variation was shown to be low during standard culture, as clonality of U2OS cells is maintained after single-cell cloning and continuous culture for months [Irianto et al. Curr Biol 2017].

Furthermore, there were zero loss of heterozygosity and SNV calls from the Y chromosome, which is consistent with derivation of the U2OS line from a female patient. Likewise, when these U2OS cells were subjected to RNA sequencing, there were zero reads of mRNA from the Y chromosome; in contrast, 40%–57% of genes from all other chromosomes are expressed [Irianto et al. Curr Biol 2017].

Mycoplasma contamination

The U2OS cell line used in our study tested negative for mycoplasma contamination.

Commonly misidentified lines
(See ICLAC register)

No commonly misidentified cell lines were used.